Single-Cell Map of Dynamic Multicellular Ecosystem of Radiation-Induced Intestinal Injury

Short title: Single-cell map of dynamic ecosystem of RIII

Hua Yan[1,4], Hao Lu[1,4], Yuan Xing[1], Yumeng Ye[1], Siao Jiang[1], Luyu Ma[1], Hongyan Zuo[1], Yanhui Hao[1], Chao Yu[1], Yang Li[1,2,*], Yiming Lu[1,*], Gangqiao Zhou[1,3,*]

Affiliations:

[1]Beijing Institute of Radiation Medicine, Beijing 100850, China;

[2]Academy of Life Sciences, Anhui Medical University, Hefei City, Anhui Province, 230032, China;

[3]Collaborative Innovation Center for Personalized Cancer Medicine, Center for Global Health, School of Public Health, Nanjing Medical University, Nanjing City, Jiangsu Province, 211166, China.

[4]These authors contributed equally: Hua Yan, Hao Lu.

[*]**To whom the correspondence should be addressed:**

Dr. Gangqiao Zhou, Department of Genetics & Integrative omics, State Key Laboratory of Proteomics, National Center for Protein Sciences, Beijing Institute of Radiation Medicine, 27 Taiping Road, Beijing, 100850, P. R. China. E-mail: zhougq114@126.com; Phone & fax: 86-10-66931201.

23 OR

24 Dr. Yiming Lu, Department of Genetics & Integrative omics, State Key Laboratory of

25 Proteomics, National Center for Protein Sciences, Beijing Institute of Radiation

26 Medicine, 27 Taiping Road, Beijing, 100850, P. R. China. E-mail:

27 ylu.phd@gmail.com; Phone & fax: 86-10-66930297.

28 OR

29 Dr. Yang Li, Department of Experimental Pathology, Beijing Institute of Radiation

30 Medicine, Beijing 100850, P. R. China. E-mail: leeyoung109@hotmail.com; Phone &

31 fax: 86-10-66930232.

32

Abstract

Intestine is a highly radiation-sensitive organ that could be injured during the radiotherapy for abdominal or pelvic cavity tumors. However, the dynamic change of the intestinal microenvironment related to radiation-induced intestine injury (RIII) is still unclear. Using single-cell RNA sequencing, we pictured a dynamic landscape of the intestinal microenvironment during RIII and regeneration. We showed that the multicellular ecosystem of intestine exhibited heterogeneous radiosensitivities. We revealed the distinct dynamic patterns of three subtypes of intestinal stem cells (ISCs), and the cellular trajectory analysis suggested a complex interconversion pattern among them. For the immune cells, we found that *Ly6c*$^{+}$ monocytes can give rise to both pro-inflammatory macrophages and resident macrophages after RIII. Besides, through cellular communication analysis, we identified a positive feedback loop between the macrophages and endothelial cells, which could amplify the inflammatory response induced by radiation. Overall, our study provides a valuable single-cell map of the dynamic multicellular ecosystem during RIII and regeneration, which may facilitate the understanding of the mechanism of RIII.

KEYWORDS: Radiation-induced intestinal injury; Single-cell sequencing; Intestinal stem cell; Radiation-induced inflammation.

52 **INTRODUCTION**

53 As one of the most sensitive organs to ionizing radiation, intestine could be damaged
54 during the radiotherapy for abdominal or pelvic cavity tumors or uncontrolled release
55 of radioactive materials, which would lead to radiation-induced intestinal injury (RIII).
56 Treatments of RIII are very limited and generally focused on reducing symptoms, and
57 the curative effects are not satisfactory. RIII is largely defined as clonogenic cell death
58 and apoptosis in the crypt cells, which results in insufficient replacement of villus
59 epithelium, breakdown of the mucosal barrier[1, 2], inflammation and immune
60 abnormality[3]. Previous studies mainly focused on the roles of molecules and pathways
61 in DNA damage, apoptosis, autophagy[4], inflammation and immune. However, the
62 dynamics of the microenvironment during intestine injury and regeneration remains
63 poorly understood, which limits the elucidation and treatment of RIII. Therefore, the
64 present study aims to clarify the dynamic variation of the cellular microenvironment
65 of RIII.

66 It has been widely accepted that the intestinal stem cells (ISCs) are able to
67 replenish the whole crypt–villus axis, generating all differentiated cell types required
68 for the physiological function of the intestine[5]. A number of ISC subpopulations in the
69 small intestine have been identified, including Lgr5+ crypt-based columnar cells
70 (CBCs), +4 reserve stem cells (RSCs) and revival stem cells (revSCs). Lgr5+ CBCs
71 are considered indispensable for intestine recovery following exposure to radiation[6].
72 +4 RSCs, which express specific markers *Bmi1*, *Hopx* and *Tert*[7-9], have been
73 described as a slow dividing reserve stem cell population. Recently, a group of

74 revSCs was identified to be extremely rare under homoeostatic conditions and arise in
75 damaged intestines to reconstitute Lgr5+ ISCs and regenerate the intestine[10].
76 Irradiation causes a sharp reduction in the number of ISCs, which brings great
77 challenges in the repair of injured intestinal epithelium. Despite the advances in our
78 understanding of the ISCs in the past few years, a dynamic landscape of ISCs during
79 injury and regeneration is still lacking and their interconversion relationships remain
80 puzzling.

81 Immune cells also play important roles in the pathogenesis of RIII. Macrophages
82 are crucial component of the immune system in the intestine, which modulate
83 inflammation by secreting distinct cytokines and acting as professional
84 phagocytes[11-13]. Intestinal macrophages require continuous replenishment by blood
85 monocytes and have very poor proliferative capacity, which is different from the other
86 tissue macrophages. Exposure to radiation can significantly decreases the levels of
87 macrophages in the damaged intestine[14]. Besides, the elucidation of the role of
88 cross-talk between the macrophages and other cells in the initial inflammatory
89 response and microenvironment homeostasis recovery post irradiation is also of great
90 significance for the development of new therapeutic targets.

91 Recently, the single-cell RNA sequencing (scRNA-seq) has been applied to
92 identify new cell types or cell states[15-17], investigate cellular plasticity and stemness of
93 ISCs[10, 18], or trace developmental relationships among different cell populations in the
94 intestine[19]. However, these studies have not investigated the dynamic changes of
95 microenvironment during intestine injury and regeneration. Here, we utilized the

96 scRNA-seq to explore the multicellular ecosystem of homeostatic and regenerating
97 intestine in a time-course manner. We generated transcriptomes of 22,680 single cells
98 in the intestinal microenvironment, trying to profile the dynamics of ISCs and
99 immune cells located in the mucous layer. This large-scale single-cell transcriptome
100 data can be used as a valuable resource for further studying the cellular mechanism of
101 RIII and development of potential therapy strategies.

102 **RESULTS**

103 **A dynamic single-cell map of multicellular ecosystem in healthy and injured**
104 **small intestine**

105 Mice were exposed to 15 Gy of abdominal irradiation using a Co^{60} irradiator to induce
106 intestinal injury (Figure 1A). About 20% mice died in the irradiation group within 3-6
107 days post-irradiation (Figure 1B). The body weights of mice after irradiation exposure
108 continued to lose in the first 7 days and then gradually increased afterward (Figure
109 1C). In line with this, exposed mice showed significantly reduced intestinal weight at
110 day 3 and day 7 post-irradiation as compared to unexposed mice and showed recovery
111 at day 14. Morphological and cellular phenotype analyses also showed significant
112 decrease of villus length, villus width, crypt depth and number of crypts at day 1
113 and/or day 3 post-irradiation (Figures S1A–S1D). A peak of TUNEL-positive cells at
114 day 1 post-irradiation suggested that the radiation-induced cell death occurs mostly
115 within the first 24–48 hours (Figure S1E). An increase of Ki-67-positive cells from
116 day 3 to day 14 indicated that the day 3–14 is a key time-window for intestinal
117 regeneration (Figure S1F).

118 To generate a dynamic single-cell map of the intestinal microenvironment related
119 to RIII, we employed a droplet-based scRNA-seq approach to profile the
120 transcriptomes of single cells from the intestinal tissues at day 1 (n = 4), day 3 (n = 3),
121 day 7 (n = 3) and day 14 (n = 3) after irradiation exposure as well as the unexposed
122 healthy intestinal tissues (n = 4) (Figure 1A). After quality filtering, we obtained the
123 transcriptomes of a total of 22,680 single cells, with an average of 1,778 genes and
124 7,843 unique transcripts per cell (Figures S2A and S2B; Table S1). These
125 transcriptomes of single cells from all samples were merged using a canonical
126 correlation analysis (CCA)-based batch correction approach to generate a global map
127 of cellular microenvironment of healthy and injured intestines. Shared nearest
128 neighbor (SNN) graph-based clustering of single cells identified a total of 54 cell
129 clusters (subtypes), which were visualized on the t-distributed stochastic neighbor
130 embedding (t-SNE) dimensional reduction map (Figures 1D, S2C and S2D).
131 Differentially expressed genes were calculated for each cell cluster using the
132 Wilcoxon rank sum test.
133 Using canonical marker genes, we identified 10 major cell types in our dataset,
134 including intestinal stem cells (ISCs), transit amplifying (TA) cells, enterocytes,
135 goblet cells, enteroendocrine cells (EECs), Paneth cells, endothelial cells, T cells, B
136 cells and myeloid cells, and most of them consist of multiple subtypes (Figures 1E
137 and S2E), suggesting a complex cellular ecosystem of healthy and irradiation-injured
138 intestines. We found the intestinal ecosystem changed greatly during RIII and
139 regeneration (Figure 1F and 1G). Specifically, the stem cells and immune cells (T

140 cells, B cells and myeloid cells) decreased markedly at day 1 post-irradiation;
141 enterocytes decreased sharply at day 3; and immune cells and endothelial cells
142 exhibited a dramatic increase at day 3. Despite of the great alterations of intestinal
143 microenvironments during the first 7 days post-irradiation, intestinal tissues at day 14
144 exhibited very similar cellular composition with those non-irradiated ones. These
145 results suggested that intestinal multicellular ecosystem disrupted by intense
146 abdominal irradiation can be largely reconstructed within 14 days post-irradiation,
147 which is in line with our morphological observations (Figure S1).

148 **Intestinal multicellular ecosystem showed heterogeneity of *in vivo***
149 **radiosensitivities**

150 The dynamic change of cellular composition in intestines before and after irradiation
151 exposure provided an opportunity to explore the *in vivo* radiosensitivities of various
152 cell subtypes. To quantify the radiosensitivity for each cell cluster, we compared the
153 ratios between the observed and expected cell numbers from the intestinal samples at
154 day 1 after irradiation. Consistent with previous studies[6, 20], most ISC and immune
155 cell subtypes are highly radiosensitive, exhibiting significantly lower frequencies than
156 expected at day 1 (Figure 2A). Nevertheless, there are a few ISC and immune cell
157 subtypes (C22, C30, C19 and C35) exhibited similar or higher frequencies than
158 expected at day 1, suggesting they are radioresistant subpopulations. Apart from ISCs
159 and immune cells, we found all the endothelial and stromal cell subtypes are
160 radioresistant, while the enterocytes, goblet cells and EECs exhibit heterogeneous
161 levels of radiosensitivity across their respective subtypes.

162 We next sought to identify the pathways activated by various cell types to
163 confront irradiation-induced apoptosis. We focused on the top four enriched major cell
164 types in our dataset, including the ISCs, enterocytes, myeloid cells and T cells. For
165 each cell type, we identified pathways significantly up-/down-regulated in surviving
166 cells at day 1 post-irradiation using the whole cells from non-irradiated samples as
167 background (Figures 2B, 2C and S3). Notably, a number of pathways, including
168 PI3K/AKT/mTOR signaling, MYC signaling, TGF-β signaling and cell cycle-related
169 pathways, were consistently downregulated in surviving cells of different cell types,
170 while KRAS-down signaling pathway were consistently upregulated in surviving cells.
171 We also investigate the genes that are upregulated in survived cells at day 1
172 post-irradiation as compared to non-irradiated cells for the stem cells, enterocytes,
173 myeloid cells and T cells, respectively. We identified 67 significantly upregulated
174 genes that were shared by all the major cell types (Figures 2D and 2E). Functional
175 annotation showed that the upregulated genes include several genes known to be
176 involved in the negative regulation of apoptotic process (Table S3).

177 **Dynamics of three distinct ISC subpopulations during intestinal injury and**
178 **regeneration**

179 ISCs are critical for epithelium regeneration after injury[6, 10]; however, their
180 phenotypic heterogeneity and dynamics during intestinal injury and regeneration have
181 not been fully characterized. We identified a total of 2,411 ISCs that were divided into
182 five clusters (Figures 3A, 3B and S4). Cells in clusters C4, C9, and C16 highly
183 expressed *Lgr5*$^{+}$ CBC signatures (*Olfm4*, *Smoc2* and *Prom1*), suggesting they are

184 *Lgr5*$^{+}$ CBCs; stem cells in C35 expressed high levels of +4 RSC signatures (*Hopx* and
185 *Tert*), suggesting they are a set of +4 RSCs[21, 22]; cluster C28 was enriched for stem
186 cells that highly expressed *Clu*, *Cxadr* and *Anxa1*, which are signatures of recently
187 reported *Clu*$^{+}$ revSCs[10]. We found *Clu*$^{+}$ revSCs in C28 also showed high expression
188 levels of cell cycle-related genes. A closer examine of cells in cluster C28 reveals two
189 different subclusters (C28a and C28b). Cells in C28a expressed higher levels of *Clu*
190 and lower levels of cell cycle-related genes, indicating they are likely to be quiescent
191 *Clu*$^{+}$ revSCs. On the contrary, cells in C28b expressed lower levels of *Clu* and higher
192 levels of cell cycle-related genes, suggesting that a portion of *Clu*$^{+}$ revSCs may be in
193 actively proliferating status during RIII.

194 We then investigated the temporal dynamics of these ISC subpopulations. The
195 proportion of *Lgr5*$^{+}$ CBCs was drastically reduced at day 1 and day 3 and was
196 substantially recovered at day 14 post-irradiation (Figure 3C). In line with the
197 scRNA-seq data, the integral luminous density of *in situ* hybridization with probes
198 specific for *Olfm4* showed similar results (Figure 3D). By contrast, +4 RSCs in C35
199 were specifically enriched at day 1 post-irradiation, suggesting they are not only
200 radioresistant but can also be induced by irradiation (Figure 3C), in line with a
201 previous study that detected increased lineage tracing output of +4 RSCs after
202 irradiation exposure[23]. Distinct from *Lgr5*$^{+}$ CBCs and +4 RSCs, *Clu*$^{+}$ revSCs in C28
203 were specifically enriched at day 3 post-irradiation (Figure 3C), in accordance with
204 the study that first reported the population of *Clu*$^{+}$ revSCs[10]. Collectively, these results
205 showed the distinct dynamic patterns of three ISCs subpopulations. Moreover, the

206 temporal sequential enrichment of +4 RSCs, *Clu*$^+$ revSCs and *Lgr5*$^+$ CBCs during this
207 process hints at a potential sequential differentiation relationship among them.

208 **Differentiation trajectory analyses of intestinal stem cell subpopulations**

209 We next sought to explore the differentiation trajectories among these heterogeneous
210 ISC subpopulations. RNA velocity has recently emerged as a powerful approach for
211 inferring the transition direction of a single cell to neighboring cells[24]. Here, we
212 performed RNA velocity analysis on stem cell populations in a time-course manner.
213 Given that only +4 RSCs were enriched at day 1, we combined them with ISCs
214 presented under homeostatic conditions (Control-D1) or those presented at day 3
215 (D1-D3), respectively, to investigate the inter-subpopulation differentiation
216 trajectories. Notably, the Control-D1 RNA velocity map showed that there is a
217 velocity flow from *Lgr5*$^+$ CBCs toward +4 RSCs (Figure 3E), in accordance with a
218 previous study that demonstrated the interconversion between *Lgr5*$^+$ CBCs and +4
219 RSCs[9]. This result may explain the specific enrichment of +4 RSCs at day 1
220 post-irradiation. We observed two clear velocity flows in the D1-D3 map (Figure 3F).
221 The first flow initiates from the +4 RSCs toward *Clu*$^+$ revSCs, suggesting +4 RSCs
222 may be able to differentiate to *Clu*$^+$ revSCs. This result is not only in accordance with
223 the specific enrichment of *Clu*$^+$ revSCs at day 3 post-irradiation rather than at day 1
224 (Figure 3B), but also consistent with the observation of a peak of CLU-tdTomato$^+$
225 clone frequency at the +4 position from the crypt bottom[10], where +4 RSCs are
226 specifically enriched. The second flow is from the *Clu*$^+$ revSCs toward *Lgr5*$^+$ CBCs,
227 suggesting that *Clu*$^+$ revSCs could repopulate *Lgr5*$^+$ CBCs when the latter were

228 almost eliminated by irradiation, in line with the previous study[10].

229 We then used SCENIC[25] to investigate the potential key regulons along these
230 velocity flows. We found Myc and Hdac1 were among the top transcription factors
231 (TFs) that exhibit significantly increasing activities along the velocity flow from
232 *Lgr5*$^+$ CBCs toward +4 RSCs (Figure 3G). Myc has been reported to be required for
233 intestinal formation and regeneration but dispensable for homeostasis of the adult
234 intestinal epithelium[26, 27]. Here, our result suggested Myc may facilitate intestinal
235 regeneration by promoting the conversion from *Lgr5*$^+$ CBCs to +4 RSCs upon
236 radiation-induced injury. Besides, Hdac1 was also reported to regulate intestinal stem
237 cell homeostasis[28]. Among the top correlated TFs along the velocity flow from +4
238 RSCs toward *Clu*$^+$ revSCs (Figure 3H), Ybx1 is a stress-activated TF and has been
239 reported to be able to transcriptionally activate *Clu* expression by directly binds to the
240 promoter regions of *Clu*[29]. Our data suggest Ybx1 may play important roles in the
241 induction of *Clu*$^+$ revSCs from +4 RSCs. Besides, another TF Hmga1 has been
242 reported to amplify the Wnt signaling and expand the intestinal stem cell
243 compartment and Paneth cell niche[30]. For the velocity flow from *Clu*$^+$ revSCs toward
244 *Lgr5*$^+$ CBCs, we found Runx1 and Stat3 were among the top correlated TFs (Figure
245 3I). Stat3 has been shown to be indispensable for damage-induced crypt
246 regeneration[31] and the Runx1-Stat3 signaling pathway has been reported to regulate
247 the differentiation of *Lgr5*$^+$ CBC[32]. Taken together, our results revealed the possible
248 differentiation trajectories among *Lgr5*$^+$ CBCs, +4 RSCs and *Clu*$^+$ revSCs upon
249 intestinal injury, and identified the specific TF sets driving these differentiation paths.

250 **Bidirectional differentiation of peripheral monocytes into pro-inflammatory**
251 **macrophages and resident macrophages**
252 A total of 4,010 myeloid cells were identified in our dataset, which were divided into
253 five clusters (C0, C22, C24, C36 and C38) (Figure 4A). Cells in cluster C0 expressed
254 high levels of monocyte markers (*Cd14*, *Ccr2* and *Ly6c2*), indicating they are
255 peripheral *Ly6c*$^+$ monocytes. Cells in C22 highly expressed macrophage markers
256 (*Cd80*, *Cd206*, *Cd64* and *F4/80*) and a set of pro-inflammatory genes (*Il1a*, *Il1b*, *Il6*
257 and *Tnf*), suggesting they are a set of pro-inflammatory macrophages. C36 was
258 enriched for cells expressed high levels of resident macrophage markers (*Cx3cr1* and
259 *Fcgr1*), suggesting they are *Cx3cr1*$^+$ resident macrophages. Besides, we also
260 identified a cluster of neutrophils (C24) highly expressing neutrophil markers (*Ly6g*,
261 *Retnlg* and *S100a9*) (Figure 4B).
262 We then investigated the temporal distribution of these myeloid subpopulations.
263 We found that *Ly6c*$^+$ monocytes (C0), pro-inflammatory macrophages (C22) and the
264 neutrophils (C24) were highly enriched at day 3 post-irradiation (Figure 4C). The
265 temporal distributions of pro-inflammatory macrophages after irradiation were
266 confirmed by flow cytometry, and their expression of pro-inflammatory cytokines
267 were measured (Figures 4D-4F). In contrast, *Cx3cr1*$^+$ resident macrophages in C36
268 showed depletion at day 1 and day 3 post-irradiation and became abundant at day 7,
269 suggesting resident macrophages are radiosensitive and could rapidly recover after
270 irradiation.
271 Using RNA velocity analysis, we found that there are two differentiation paths

272 initiated from *Ly6c*$^{+}$ monocytes towards pro-inflammatory macrophages and *Cx3cr1*$^{+}$
273 resident macrophages, respectively (Figure 4G). Although the alternative outcomes of
274 *Ly6c*$^{+}$ monocytes to be resident and pro-inflammatory macrophages has been
275 previously reported in inflammatory bowel disease (IBD)[33], our result shows that this
276 bidirectional differentiation pattern may be import for RIII recovery. Further, SCENIC
277 analysis was performed to investigate the potential key regulons driving these two
278 differentiation paths, respectively. We found these two differentiation paths shared
279 several top correlated TFs, including Cebp, Maf, Mafb and Nr1h3 (Figure 4H and 4I).
280 CCAAT/enhancer-binding protein (Cebp), Maf and Mafb transcription factors has
281 been reported to be important for monocyte-to-macrophage differentiation[34]. Nuclear
282 receptor Nr1h3 (LXRα) has also been reported to be a major regulator of macrophage
283 development[35]. Besides the shared TFs, the two differentiation paths were also driven
284 by specific factors. Activities of Jun, Stat1, Irf1 and Irf2 were specifically upregulated
285 along the velocity flow from *Ly6c*$^{+}$ monocytes to pro-inflammatory macrophages
286 (Figure 4H), while Myc and Myc-associated zinc finger (Maz) were specifically
287 upregulated along the velocity flow from *Ly6c*$^{+}$ monocytes to resident macrophages
288 (Figure 4I), in accordance with the key role of Myc in the self-renewal activity of
289 macrophages[36]. Together, these results suggested that peripheral monocytes could
290 differentiate into both pro-inflammatory macrophages and resident macrophages after
291 RIII, and these two differentiation paths may be driven by different key TFs.

292 **A positive feedback loop between the macrophages and endothelial cells**
293 **amplifies inflammatory response upon RIII**

294 To assess the roles of various cell types in the inflammatory response induced by
295 irradiation, we investigated the ligand-receptor (L-R) pairs that mediate cellular
296 interactions among the cell clusters. A total of 2,064 L-R interactions were identified
297 among all the cell clusters within the intestinal microenvironment. We found the
298 cellular interacting patterns varied greatly at different times during RIII and recovery
299 (Figure 5A). Especially, we observed massive interactions that occur between the
300 macrophages and endothelial cells at day 3 post irradiation, in contrast to other time
301 points and other cell types.

302 We found that the activated endothelial cells expressed high levels of adhesion
303 molecules such as *Vcam1* and *Icam1*, to recruit pro-inflammatory macrophages, in
304 accordance with previous studies[37]. Besides the adhesion molecules, we found these
305 endothelial cells also expressed high levels of chemokine *Cxcl12* to recruit
306 pro-inflammatory macrophages (Figure 5D). Interestingly, the pro-inflammatory
307 macrophages expressed high levels of vascular endothelial growth factor (*Vegf*),
308 which could, in turn, enhance the endothelial cell survival and proliferation[38] (Figure
309 5D). The interactions between the activated endothelial cells and pro-inflammatory
310 macrophages could amplify the proliferation of both populations, which is consistent
311 with the specific enrichment of pro-inflammatory macrophages and endothelial cells
312 at day 3 post irradiation. We speculate the amplification effect is critical for the quick
313 induction of inflammation at early stage of intestinal injury.

314 We also sought to identify the pathways that are upregulated upon endothelial
315 cells activation during RIII. Compared to endothelial cells in homeostatic intestine,

316 the activated endothelial cells at day 3 post irradiation were shown to be upregulated
317 in inflammatory response, TNF-α signaling via NF-κB, EMT and KRAS signaling
318 pathways (Figures 5B and 5C). NF-κB has been reported to play a pivotal role in the
319 inducible expression of cytokines in inflammatory response induced by irradiation[39].
320 Besides, we found KRAS signaling pathway may also play an important role in
321 inflammatory cytokines induction. In addition, the upregulation of EMT pathway
322 indicates that irradiation could induce the epithelial-to-mesenchymal transition of
323 endothelial cells, which may be involved in intestinal fibrosis after radiation
324 exposure[40]. Collectively, these results showed that the cellular interactions between
325 macrophages and endothelial cells could achieve a quick amplification of
326 inflammation upon the RIII.

327 **DISCUSSION**

328 The dynamics of cellular microenvironment during the radiation-induced intestinal
329 injury and regeneration remains largely uncharacterized. In this study, by combining
330 the single-cell transcriptome profiling with temporal distribution analysis, lineage
331 reconstruction, TF profiling and cellular interaction analyses, we provided a
332 comprehensive dynamic landscape of the cellular microenvironment during intestinal
333 injury and regeneration.

334 The radiosensitivity of cells varies greatly, mainly depending on the degree of
335 cell differentiation, cell proliferation ability, metabolic status and surrounding
336 environment[3, 41]. Currently, it is widely accepted that the lymphocytes, hematopoietic
337 cells, small intestinal crypt cells and germ cells are highly radiosensitive cell types,

338 but these kinds of cells are composed with multiple subtypes with different biological
339 characteristics. In this study, based on scRNA-seq, we assessed the *in vivo*
340 radiosensitivity of different cell subtypes in the intestinal microenvironment. Our data
341 not only showed that diverse cell subtypes in the intestinal microenvironment
342 exhibited highly heterogeneous levels of radiosensitivity, but also revealed cross-cell
343 consistency of pathway activation for various cell types to confront the
344 radiation-induced apoptosis.

345 Much attention has been focused on ISC injury and regeneration post irradiation[6,
346 10, 23, 42]. It is generally accepted that Lgr5+ stem cells were sensitive to irradiation
347 injury while +4 stem cells show relatively lower sensitivity[7, 9, 23], we here reported a
348 comprehensive survey on the phenotype and dynamics of diverse ISC subsets in
349 different phases after high-dose irradiation. Generally, we identified three
350 subpopulations of ISCs, including *Lgr5*$^{+}$ CBCs, +4 ISCs as well as a cluster of *Clu*$^{+}$
351 revISCs reported recently[10], with distinct dynamic characteristics. Additionally, our
352 data provides new insights into the interconversion relationships among the three ISC
353 subpopulations. Although a previous study has shown *Lgr5*$^{+}$ CBCs could give rise to
354 +4 RSCs in culture[9], our data suggests this conversion could be induced *in vivo* by
355 intestinal injury. Besides, we also showed that *Clu*$^{+}$ revISCs may originate from *Lgr5*$^{+}$
356 CBCs and +4 revISCs, although further studies are still needed to test and verify the
357 transformation processes.

358 Exposure to irradiation could also strongly affect immune system responses in the
359 intestine, which were essential for maintaining mucosal homeostasis. In this study, we

360 observed that *Cx3cr1*$^{+}$ resident macrophages are drastically reduced at 1 day
361 post-irradiation and were then followed by a massive influx of monocytes and
362 macrophages into the injured intestine. Our data suggested that the bidirectional
363 differentiation of peripheral *Ly6c*$^{+}$ monocytes to pro-inflammatory macrophages or
364 *Cx3cr1*$^{+}$ resident macrophages may be important for balancing the radiation-induced
365 inflammation and resident macrophages recovery. We also showed that different TFs
366 may contribute to the alternative fates of *Ly6c*$^{+}$ monocytes, which could be potential
367 intervention targets for modulating the early stage inflammation induced by radiation.
368 In addition, we found the cellular interacting patterns varied greatly at different
369 times during RIII and recovery; especially, the massive interactions between the
370 macrophages and endothelial cells at early inflammation stage aroused our attention.
371 Our results showed that the cross-talk between pro-inflammatory macrophages and
372 activated endothelial cells could achieve a quick amplification of inflammation upon
373 RIII. This finding suggested that intervention in the interaction between these two
374 cells might alleviate early inflammation.
375 In summary, based on scRNA-seq, our research refined the radiosensitivity of
376 small intestinal cells in the cell subtype level. Besides, our dataset revealed the
377 dynamic patterns of three ISC subpopulations and their interconversion relationships.
378 Additionally, we showed the bidirectional differentiation of peripheral monocytes into
379 pro-inflammatory macrophages and resident macrophages, and the amplifying
380 communicating relationships between macrophages and endothelial cells during the
381 inflammatory response upon RIII. These findings may provide new views on the

382 cellular and molecular mechanisms of RIII.

383 **MATERIALS AND METHODS**

384 **Ethics statement**

385 The study was approved by the institutional review board of Beijing Institute of
386 Radiation Medicine (protocol ID: IACUC-DWZX-2020-623). The work submitted in
387 this article was solely completed by the teams of Gangqiao Zhou, Yiming Lu and
388 Yang Li, and it is original. Excerpts from others' work have been clearly identified
389 and acknowledged within the text and listed in the list of references.

390 **Mice and groups**

391 Wild-type male C57BL/6J mice (weight of 20 ± 2g) were purchased from Beijing
392 Vital River Laboratory Animal Technology Co., Ltd. (Beijing, China). All the mice
393 were bred in a specific pathogen-free environment under conditions of constant
394 temperature of 22 ± 1°C, relative humidity of 60%, and regular dark-light schedule
395 (lights on from 7 a.m. to 7 p.m.) at the Experimental Animal Center of the Beijing
396 Institute of Radiation Medicine, China. A total of 97 mice were used in this study,
397 including 78 random mice receiving abdominal irradiation and 19 random mice as
398 negative controls. The irradiation exposed mice were then randomly divided into four
399 groups and intestinal samples were collected and used for experiments at day 1, 3, 7
400 and 14 post-irradiation, respectively. Specifically, 17 mice were used for scRNA-seq
401 (n = 3 or 4 for each group), 20 mice for flow cytometry (n = 3 for each group, with
402 additional 5 mice for flow cytometry cell sorting at day 3), 30 mice for
403 immunohistochemistry (n = 6 for each group), and 30 mice for *in situ* hybridization

404 analyses (n = 6 for each group).

405 **Abdominal irradiation of mice**

406 Mice were anaesthetized with an intraperitoneal injection of 0.5% pentobarbital (43
407 mg/kg body weight) and exposed to a single dose of 15 gray (Gy) abdominal
408 irradiation (from the xiphoid process to the pubic symphysis with lead bricks to cover
409 the other parts of the mice) using a Co^{60} irradiator to induce intestinal injury *in vivo*.
410 All experiments were repeated at least twice with n = 6 mice in each group, except for
411 the scRNA-seq, in which each group contain n = 3 or 4 mice. Mice were monitored
412 for up to 15 days, and the changes in small intestine lengths and weights were
413 recorded on day 0, 1, 3, 7, 14 post-irradiation.

414 **Morphological analyses of mice villus and crypt**

415 Mice were monitored for up to 15 days. The mice in control and irradiation groups
416 were sacrificed on day 1, 3, 7, 14 following irradiation, and the intestine tissues were
417 harvested and fixed in a 10 % neutral buffered formalin solution. The fixed samples
418 were dehydrated, cleared and permeated with paraffin in a tissue processor, and
419 subsequently embedded in paraffin blocks using an embedding system.
420 Paraffin-embedded samples were sectioned at a 5-mm thickness and stained with
421 hematoxylin & eosin (HE) staining. The slides were imaged at 50 ×, 100 × and 400 ×
422 magnification, respectively, using an Olympus BX51 microscope (Japan). The villus
423 length and width, crypt depth, thickness of muscular layer and number of crypts per
424 intestinal length were measured with ImageJ (NIH). The villus length was measured
425 from the top to the base of the villus at the entrance to the intestinal crypt. The villus

426 width was measured at half of its length. The crypt depth was measured from the
427 depth of the invagination to the adjacent villi. For each group, at least 30
428 well-oriented villi were measured and the mean value was calculated.

429 **Single-cell sequencing library construction**

430 To isolate single cells, duodenums were amputated (about 5 cm beyond the pylorus)
431 and 10 cm jejunum segments following the incision of the mice on day 0, 1, 3, 7, 14
432 after irradiation were washed in cold PBS, cut longitudinally into roughly 2-mm-long
433 pieces and were isolated using the Liver Dissociation Kit (mouse) and GentleMACS
434 Dissociator (Miltenyi Biotec, Germany) according to the manufacturer's instructions.
435 Tissues were filtered through a 40-μm-mesh cell strainer on ice, pelleted by
436 centrifugation at 4 °C and washed twice with the ice-cold regular medium to remove
437 the debris. An estimated 5,000 single cells per sample were then subjected to 10x
438 Genomics single-cell isolation and RNA sequencing following the manufacturer's
439 recommendations. Illumina HiSeq 3000 was used for deep sequencing. Two technical
440 replicates were generated per sorted cell suspension.

441 **Analysis of scRNA-seq data**

442 The Cell Ranger software (version 2.2.0) provided by 10x Genomics was used to
443 align the reads from droplet-based scRNA-seq to an indexed mouse genome (mm10,
444 NCBI Build 38), generating a digital gene expression matrix (UMI counts per gene
445 per cell) for each sample. Expression matrices for all samples were filtered,
446 normalized, integrated and clustered using the standard Seurat (version 2.3.4) package
447 procedures. More exactly, for the first quality-control (QC) step, we removed the

448 genes detected in less than three cells and cells with below 500 or over 8,000
449 expressed genes and over 10% UMIs derived from mitochondrial genome. After
450 applying these QC criteria, a total of 22,680 cells and 19,588 genes in total remained
451 and were included in the following analyses. Then the expression matrices were
452 log-normalized and scaled to remove the unwanted variation from the total cellular
453 read count and mitochondrial read count, as implemented in Seurat's *NormalizeData*
454 and *ScaleData* functions. To integrate datasets from different samples, we used a
455 subset of highly variably expressed genes to perform the canonical correlation
456 analysis (CCA). First, the top 1,000 genes with the largest dispersion in each dataset
457 were selected; then the genes from all 17 datasets were intersected to determine an
458 overlap-gene set. We used the overlap-gene set as variable genes to implement CCA
459 through Seurat's *RunMultiCCA* function, which returned an integrated Seurat objects
460 with canonical correlation vectors. Seurat's *AlignSubspace* function was employed to
461 align the top ten dimensions in CCA subspaces and generate the *cca.aligned*
462 dimensional reduction. With the first ten components of the dimensional reduction,
463 we then performed a shared nearest neighbor (SNN) modularity optimization
464 clustering method with the Louvain algorithm as implemented in the *FindClusters*
465 function, which finally identified 54 clusters of different cell types or subtypes, and
466 different clusters of cells were visualized using a further t-distributed Stochastic
467 Neighbor Embedding (tSNE) dimensionality reduction.

468 **Immunohistochemistry assay**

469 The 5 μm thick sections from the paraffin-embedded small intestine sections were

470 deparaffinized and rehydrated using xylene and ethanol, and boiled for 15 minutes
471 (min) in 10 mM citrate buffer solution (pH 6.0) for antigen retrieval. The sections
472 were then immersed in a 3% hydrogen peroxide solution for 10 min to block the
473 endogenous peroxidase. Slides were incubated with goat serum for 10 min and then
474 with the primary antibody anti-Ki67 (#ab16667, 1:200; Abcam). A horse radish
475 peroxidase (HRP)-based signal amplification system was then hybridized to a goat
476 anti-rabbit IgG (H&L) secondary antibody (#PV9001; ZSBIO) followed by
477 colorimetric development with diaminobenzidine (DAB). Positive cells were counted
478 in the crypt and villi at 30 randomly selected position per group with ImageJ.

479 **TUNEL assay**

480 Apoptotic cells were identified by terminal deoxynucleotidyl transferase-mediated
481 dUTP nick end-labeling (TUNEL) staining using the *In Situ* Cell Death Detection Kit
482 (Roche) according to the manufacturer's protocol. Briefly, the paraffin-embedded
483 sections were prepared the same as hematoxylin & eosin (HE) staining. After drying
484 and deparaffinized, the section was treated by proteinase K (20 μg/mL; Roche, Swiss)
485 for l0 min to make the cell membrane permeable, and then treated by the mixed
486 reaction solution for TUNEL reaction. After treatment with biotin-labeled HRP, DAB
487 chromogen was used to render the color. TUNEL-positive cells were identified and
488 their numbers were counted within a defined area (μ2) using an Olympus BX51
489 microscope (Japan).

490 ***In situ* hybridization**

491 *In situ* hybridization (ISH) assays for *Olfm4* were performed with the RNAscope kit

492 (Advanced Cell Diagnostics, California, USA) according to the manufacturer's
493 instructions. Five μm formalin-fixed, paraffin embedded tissue sections or 8 μm OCT
494 frozen were pretreated with heat and protease digestion prior to hybridization with
495 target probes (Advanced Cell Diagnostics). An HRP-based signal amplification
496 system was then hybridized to the target probes followed by colorimetric development
497 with DAB or Fitc, and Cy3. The housekeeping gene *ubiquitin C* (*UBC*) was served as
498 a positive control and the *dapB* gene, which is derived from a bacterial gene sequence,
499 was used as a negative control.

500 **Identification of marker genes**

501 To identify the marker genes for each of the 54 clusters of different cell types or
502 subtypes, we contrasted the cells from each cluster to cells from all the other clusters
503 using the Seurat's *FindMarkers* function. The marker genes were required to: (1) have
504 an averaged expression in the current cluster that is at least 0.25-fold (log-scale) larger
505 than that in all other clusters; and (2) show expression in at least 10% of cells in either
506 of the two comparative populations.

507 **Flow cytometry**

508 Single cells prepared as above were resuspended in phosphate buffered saline (PBS).
509 For macrophages, the antibodies used were against Cd45, F4/80, Cd11b and Cd14,
510 and cells were stained with 7-AAD to differentiate live cells. Antibody staining was
511 performed at RT for 30 min before washing cells twice with PBS. The 7-AAD was
512 added to the final FACS medium for 10 min before flow cytometry analyses and/or
513 isolation of required single-cell populations. These cells were gated on live cells

514 (those that were 7-AAD negative) and CD45 positivity. Subsequent determinations
515 included the presence of F4/80 and Cd11b followed by the presence or absence of
516 Cd14. The cells were analyzed on a BD FACSCanto II flow cytometer (BD, New
517 Jersey, USA) utilizing FACS Diva Software (BD).

518 **RNA velocity analyses**

519 RNA velocity of single cells was estimated as previously reported. More exactly, the
520 spliced and unspliced transcript reads were calculated based on the CellRanger output
521 using the velocyto command line tool with run10x subcommand. Transcript counts
522 from different samples were merged together and genes with an average expression
523 magnitude < 0.5 (for spliced transcripts) or < 0.05 (for unspliced transcripts) in at
524 least one of the clusters of each cell type were then removed. Cell-to-cell distance was
525 calculated using Euclidean distance based on the correlation matrix of the *cca.aligned*
526 dimensional reduction from Seurat. RNA velocity was estimated using gene-relative
527 models, with k-nearest neighbor cells pooling of 20 and fit quantile of 0.02. Velocity
528 fields were then visualized in the tSNE dimensionality reduction from Seurat.

529 **Gene set variation analysis (GSVA)**

530 To assess the relative pathway activity on the level of individual cells, we conducted
531 the gene set variation analysis (GSVA) with the GSVA package (version 1.32.0)[43].
532 The 50 hallmark gene sets (version 6.2) representing specific well-defined biological
533 states or processes were obtained from the Molecular Signatures Database
534 (MSigDB)[44], and genes in each set were converted to orthologous genes in mouse
535 with g:Profiler[45]. GSVA was performed in the *gsva* function with standard settings.

536 We then fit a linear model to the output gene set-by-cell pathway enrichment matrix,
537 implemented in the *lmFit* function of limma package (version 3.40.6), to detect the
538 differentially enriched pathways.

539 **SCENIC analysis**

540 The pySCENIC (version 0.9.11)[46] analysis was run as described for the stem cells and
541 myeloid cells. The normalized expression matrix exported from Seurat was set as the
542 input of pySCENIC pipeline. In addition, the genes with less than 200 UMI counts or
543 detected in less than 1% of the cells in the corresponding cell types were removed as
544 noise. Two transcription factor ranking databases, namely the TSS+/-10kb and
545 *500bpUp100Dw* databases, were used for inference of co-expression modules and
546 identification of direct targets. A regulon-by-cell matrix was then calculated to
547 measure the enrichment of each regulon as the area under the recovery curve (AUC)
548 of genes defining the regulon. To identify the key regulons driving the differentiation
549 trajectories among the stem or myeloid cell subpopupation, cells along each RNA
550 velocity flow were selected and their tSNE coordinates were converted using
551 principal components analysis (PCA) to capture the differentiation process on the first
552 principal component (PC1). Differential enrichment was calculated on the SCENIC
553 AUC matrix along the PC1 coordinates for each trajectory with a general additive
554 model implemented in the gam package (version 1.16.1).

555 **Ligand-receptor interaction analysis**

556 The ligand-receptor (LR) cellular interaction analysis was performed using the LR
557 pairs downloaded from Fantom5 (Ref. [47]) and CellPhone[48] databases. Ligand and

558 receptor genes were first converted to orthology genes from *homo sapiens* to *mus*
559 *musculus* by g:Profiler[45]. For genes corresponding to multiple orthology genes, we
560 selected the orthology gene with the highest mean expression across all cells. One
561 ligand or receptor was considered to be a marker ligand or receptor in one cluster if it
562 was identified as a marker gene with an average log-transformed fold-change (logFC) >
563 0.5 and an adjust *P*-value < 0.05. Two clusters were considered to interact with each
564 other if one of them was endowed with a marker ligand and the other one was
565 endowed with the corresponding marker receptor in a LR pair. For interaction analysis
566 at a specific time, only the clusters with a proportion of cells at that time > 10% were
567 included and the weighted interaction intensity between two clusters were estimated
568 by the product of the number of interacting LR pairs and the proportions of cells at
569 that time of the two. The weighted interaction intensity between two major cell types
570 was measured by summing up the pairwise weighted interaction intensity between
571 clusters from the two major cell types. The weighted interaction intensity of one
572 specific LR pair was estimated by the product of the proportions in the corresponding
573 time of the two clusters and the average logFC of the ligand and receptor in two
574 clusters.

575 **Statistical analyses**

576 GraphPad Prism 5 and R (version 3.6.0) were used to perform the statistical analyses.
577 The Kaplan-Meier method was used to analyze the animal survival curves. The
578 Chi-square test was applied to analysis the distribution of cells at different times
579 before and after irradiation. *P*-values of multiple testing were corrected by Bonferroni

580 correction method and an adjusted *P*-value < 0.05 was considered to be statistically

581 significant.

582

583 **Data availability**

584 The scRNA-seq dataset generated in this study are available at the National Center of

585 Biotechnology Information's Gene Expression Omniobus database under the

586 following accession number: GSE165318.

587

588 **REFERENCES**

589 1. Hauer-Jensen M, Wang J, Denham JW. Bowel injury: current and evolving management
590 strategies. Semin Radiat Oncol. 2003;13:357-71.
591 2. Wang J, Zheng H, Ou X, Albertson CM, Fink LM, Herbert JM, et al. Hirudin ameliorates
592 intestinal radiation toxicity in the rat: support for thrombin inhibition as strategy to minimize
593 side-effects after radiation therapy and as countermeasure against radiation exposure. J
594 Thromb Haemost. 2004;2:2027-35.
595 3. Hauer-Jensen M, Denham JW, Andreyev HJ. Radiation enteropathy--pathogenesis, treatment
596 and prevention. Nat Rev Gastroenterol Hepatol. 2014;11:470-9.
597 4. Gorbunov NV, Kiang JG. Up-regulation of autophagy in small intestine Paneth cells in
598 response to total-body gamma-irradiation. J Pathol. 2009;219:242-52.
599 5. Spit M, Koo BK, Maurice MM. Tales from the crypt: intestinal niche signals in tissue renewal,
600 plasticity and cancer. Open Biol. 2018;8.
601 6. Metcalfe C, Kljavin NM, Ybarra R, de Sauvage FJ. Lgr5+ stem cells are indispensable for
602 radiation-induced intestinal regeneration. Cell Stem Cell. 2014;14:149-59.
603 7. Montgomery RK, Carlone DL, Richmond CA, Farilla L, Kranendonk ME, Henderson DE, et
604 al. Mouse telomerase reverse transcriptase (mTert) expression marks slowly cycling intestinal
605 stem cells. Proc Natl Acad Sci U S A. 2011;108:179-84.
606 8. Sangiorgi E, Capecchi MR. Bmi1 is expressed in vivo in intestinal stem cells. Nat. Genet.
607 2008;40:915-20.
608 9. Takeda N, Jain R, LeBoeuf MR, Wang Q, Lu MM, Epstein JA. Interconversion between
609 intestinal stem cell populations in distinct niches. Science. 2011;334:1420-4.
610 10. Ayyaz A, Kumar S, Sangiorgi B, Ghoshal B, Gosio J, Ouladan S, et al. Single-cell
611 transcriptomes of the regenerating intestine reveal a revival stem cell. Nature.
612 2019;569:121-125.
613 11. Nagashima R, Maeda K, Imai Y, Takahashi T. Lamina propria macrophages in the human
614 gastrointestinal mucosa: their distribution, immunohistological phenotype, and function. J
615 Histochem Cytochem. 1996;44:721-31.
616 12. Muller AJ, Kaiser P, Dittmar KE, Weber TC, Haueter S, Endt K, et al. Salmonella gut invasion
617 involves TTSS-2-dependent epithelial traversal, basolateral exit, and uptake by
618 epithelium-sampling lamina propria phagocytes. Cell Host Microbe. 2012;11:19-32.
619 13. Rani R, Smulian AG, Greaves DR, Hogan SP, Herbert DR. TGF-beta limits IL-33 production
620 and promotes the resolution of colitis through regulation of macrophage function. Eur J
621 Immunol. 2011;41:2000-9.
622 14. Bain CC, Bravo-Blas A, Scott CL, Perdiguero EG, Geissmann F, Henri S, et al. Constant
623 replenishment from circulating monocytes maintains the macrophage pool in the intestine of
624 adult mice. Nat Immunol. 2014;15:929-937.
625 15. Grün D, Lyubimova A, Kester L, Wiebrands K, Basak O, Sasaki N, et al. Single-cell
626 messenger RNA sequencing reveals rare intestinal cell types. Nature. 2015;525:251-255.
627 16. Haber AL, Biton M, Rogel N, Herbst RH, Shekhar K, Smillie C, et al. A single-cell survey of
628 the small intestinal epithelium. Nature. 2017;551:333-339.
629 17. Glass LL, Calero-Nieto FJ, Jawaid W, Larraufie P, Kay RG, Göttgens B, et al. Single-cell
630 RNA-sequencing reveals a distinct population of proglucagon-expressing cells specific to the

631 mouse upper small intestine. Molecular metabolism. 2017;6:1296-1303.
632 18. Yan KS, Gevaert O, Zheng GXY, Anchang B, Probert CS, Larkin KA, et al. Intestinal
633 Enteroendocrine Lineage Cells Possess Homeostatic and Injury-Inducible Stem Cell Activity.
634 Cell Stem Cell. 2017;21:78-90 e6.
635 19. Herring CA, Banerjee A, McKinley ET, Simmons AJ, Ping J, Roland JT, et al. Unsupervised
636 trajectory analysis of single-cell RNA-seq and imaging data reveals alternative tuft cell origins
637 in the gut. Cell systems. 2018;6:37-51. e9.
638 20. Heylmann D, Rodel F, Kindler T, Kaina B. Radiation sensitivity of human and murine
639 peripheral blood lymphocytes, stem and progenitor cells. Biochim Biophys Acta.
640 2014;1846:121-9.
641 21. Takeda N, Jain R, LeBoeuf MR, Wang Q, Lu MM, Epstein JA. Interconversion between
642 intestinal stem cell populations in distinct niches. Science. 2011;334:1420-1424.
643 22. Montgomery RK, Carlone DL, Richmond CA, Farilla L, Kranendonk ME, Henderson DE, et
644 al. Mouse telomerase reverse transcriptase (mTert) expression marks slowly cycling intestinal
645 stem cells. Proceedings of the National Academy of Sciences. 2011;108:179-184.
646 23. Yan KS, Chia LA, Li X, Ootani A, Su J, Lee JY, et al. The intestinal stem cell markers Bmi1
647 and Lgr5 identify two functionally distinct populations. Proc Natl Acad Sci U S A.
648 2012;109:466-71.
649 24. La Manno G, Soldatov R, Zeisel A, Braun E, Hochgerner H, Petukhov V, et al. RNA velocity
650 of single cells. Nature. 2018;560:494-498.
651 25. Aibar S, González-Blas CB, Moerman T, Imrichova H, Hulselmans G, Rambow F, et al.
652 SCENIC: single-cell regulatory network inference and clustering. Nature methods.
653 2017;14:1083-1086.
654 26. Bettess MD, Dubois N, Murphy MJ, Dubey C, Roger C, Robine S, et al. c-Myc is required for
655 the formation of intestinal crypts but dispensable for homeostasis of the adult intestinal
656 epithelium. Mol Cell Biol. 2005;25:7868-78.
657 27. Kim MJ, Xia B, Suh HN, Lee SH, Jun S, Lien EM, et al. PAF-Myc-Controlled Cell Stemness
658 Is Required for Intestinal Regeneration and Tumorigenesis. Dev Cell. 2018;44:582-596 e4.
659 28. Zimberlin CD, Lancini C, Sno R, Rosekrans SL, McLean CM, Vlaming H, et al. HDAC1 and
660 HDAC2 collectively regulate intestinal stem cell homeostasis. FASEB J. 2015;29:2070-80.
661 29. Shiota M, Zoubeidi A, Kumano M, Beraldi E, Naito S, Nelson CC, et al. Clusterin is a critical
662 downstream mediator of stress-induced YB-1 transactivation in prostate cancer. Mol Cancer
663 Res. 2011;9:1755-66.
664 30. Xian L, Georgess D, Huso T, Cope L, Belton A, Chang YT, et al. HMGA1 amplifies Wnt
665 signalling and expands the intestinal stem cell compartment and Paneth cell niche. Nat
666 Commun. 2017;8:15008.
667 31. Oshima H, Kok SY, Nakayama M, Murakami K, Voon DC, Kimura T, et al. Stat3 is
668 indispensable for damage-induced crypt regeneration but not for Wnt-driven intestinal
669 tumorigenesis. FASEB J. 2019;33:1873-1886.
670 32. Sarper SE, Inubushi T, Kurosaka H, Ono Minagi H, Kuremoto KI, Sakai T, et al. Runx1-Stat3
671 signaling regulates the epithelial stem cells in continuously growing incisors. Sci Rep.
672 2018;8:10906.
673 33. Bain CC, Scott CL, Uronen-Hansson H, Gudjonsson S, Jansson O, Grip O, et al. Resident and
674 pro-inflammatory macrophages in the colon represent alternative context-dependent fates of

675 the same Ly6Chi monocyte precursors. Mucosal Immunol. 2013;6:498-510.
676 34. Lavin Y, Mortha A, Rahman A, Merad M. Regulation of macrophage development and
677 function in peripheral tissues. Nat Rev Immunol. 2015;15:731-44.
678 35. Saeed S, Quintin J, Kerstens HH, Rao NA, Aghajanirefah A, Matarese F, et al. Epigenetic
679 programming of monocyte-to-macrophage differentiation and trained innate immunity.
680 Science. 2014;345:1251086.
681 36. Soucie EL, Weng Z, Geirsdottir L, Molawi K, Maurizio J, Fenouil R, et al. Lineage-specific
682 enhancers activate self-renewal genes in macrophages and embryonic stem cells. Science.
683 2016;351:aad5510.
684 37. Francois A, Milliat F, Guipaud O, Benderitter M. Inflammation and immunity in radiation
685 damage to the gut mucosa. Biomed Res Int. 2013;2013:123241.
686 38. Gupta VK, Jaskowiak NT, Beckett MA, Mauceri HJ, Grunstein J, Johnson RS, et al. Vascular
687 endothelial growth factor enhances endothelial cell survival and tumor radioresistance. Cancer
688 J. 2002;8:47-54.
689 39. Molla M, Panes J. Radiation-induced intestinal inflammation. World J Gastroenterol.
690 2007;13:3043-6.
691 40. Mintet E, Rannou E, Buard V, West G, Guipaud O, Tarlet G, et al. Identification of
692 Endothelial-to-Mesenchymal Transition as a Potential Participant in Radiation Proctitis. Am J
693 Pathol. 2015;185:2550-62.
694 41. Kiang JG, Olabisi AO. Radiation: a poly-traumatic hit leading to multi-organ injury. Cell
695 Biosci. 2019;9:25.
696 42. Tian H, Biehs B, Warming S, Leong KG, Rangell L, Klein OD, et al. A reserve stem cell
697 population in small intestine renders Lgr5-positive cells dispensable. Nature. 2011;478:255-9.
698 43. Hanzelmann S, Castelo R, Guinney J. GSVA: gene set variation analysis for microarray and
699 RNA-seq data. BMC Bioinformatics. 2013;14:7.
700 44. Liberzon A, Birger C, Thorvaldsdottir H, Ghandi M, Mesirov JP, Tamayo P. The Molecular
701 Signatures Database (MSigDB) hallmark gene set collection. Cell Syst. 2015;1:417-425.
702 45. Raudvere U, Kolberg L, Kuzmin I, Arak T, Adler P, Peterson H, et al. g:Profiler: a web server
703 for functional enrichment analysis and conversions of gene lists (2019 update). Nucleic Acids
704 Res. 2019;47:W191-W198.
705 46. Aibar S, Gonzalez-Blas CB, Moerman T, Huynh-Thu VA, Imrichova H, Hulselmans G, et al.
706 SCENIC: single-cell regulatory network inference and clustering. Nat Methods.
707 2017;14:1083-1086.
708 47. Ramilowski JA, Goldberg T, Harshbarger J, Kloppmann E, Lizio M, Satagopam VP, et al. A
709 draft network of ligand-receptor-mediated multicellular signalling in human. Nat Commun.
710 2015;6:7866.
711 48. Vento-Tormo R, Efremova M, Botting RA, Turco MY, Vento-Tormo M, Meyer KB, et al.
712 Single-cell reconstruction of the early maternal-fetal interface in humans. Nature.
713 2018;563:347-353.

714
715

716 **Acknowledgements:**

717 This work was funded by the General Program (32270714, 81573251 and 81672369)
718 of the Natural Science Foundation of China (www.nsfc.gov.cn), Beijing Nova
719 Program (20180059), National Key R&D Program of China (No. 2017YFA0504301),
720 Chinese Key Project for Infectious Diseases (No. 2018ZX10732202 and
721 2017ZX10203205) and Beijing Institute of Radiation Medicine (BIRM) Innovation
722 Fund (BIOX0201).

723

724 **Authors contributions:**

725 G.Z., Y.Lu. and Y.Li was the principal investigators who conceived and designed the
726 study, obtained financial supports and approved the final version of the manuscript;
727 H.L., H.Y. and L.M. performed the data analyses; H.Y. conducted most of the cell
728 sorting and functional experiments; H.Y., Y.X., Y.Y., H.Z., Y.H. and C.Y. performed
729 abdominal irradiation of mice and collected intestinal samples; G.Z., Y.Lu. and Y.Li
730 drafted the manuscript. All the authors read and approved the final version of the
731 manuscript.

732

733 **Competing interests:**

734 The authors disclose no conflicts.

735

736 **FIGURE LEGENDS**

737 **Figure 1. Identification of major intestinal cell types and their markers using**
738 **scRNA-seq.** (*A*) Overview of single-cell RNA sequencing (scRNA-seq) analysis for
739 the irradiation-induced intestinal injury (RIII). (*B*) Survival rates of the mice exposed
740 to 15 Gy abdominal irradiation and in control group. (*C*) Body weights of the mice
741 exposed to 15 Gy abdominal irradiation and in control group. (*D*) tSNE projection of
742 the 22,680 cells profiled, colored by major cell types (left), Seurat cluster (upper right)
743 and experimental groups (lower right). (*E*) Heatmap displaying the z-score
744 normalized mean expression of cell type-specific canonical marker genes across
745 clusters. (*F*) Pie chart of cell type fractions in all sequenced samples. (*G*) Area chart
746 showing the dynamic changes of the proportions of major cell types in healthy
747 intestinal samples (Control) and exposed intestinal samples at different times after
748 irradiation. D1, day 1; D3, day 3; D7, day 7; and D14, day 14.
749

750 **Figure 2. Characteristics of *in vivo* radiosensitivities of different cell types in**
751 **intestine.** (*A*) Bar plots showing the fraction of cells originating from the control and
752 day 1 groups in each cluster. Only the clusters that had > 50 cells from the two groups
753 and that showed no inter-individual difference (clusters with no more than 70% of
754 cells from a single sample) were shown. Vertical dashed lines indicate the overall
755 fraction of cells originating from the control group in all shown clusters. (*B*)
756 Difference of hallmark pathway activities between stem cells from the control and day
757 1 (D1) groups. Shown are *t* values calculated in a linear modal comparing the
758 pathway scores estimated by gene set variation analysis (GSVA) between cells from
759 the two groups. (*C*) The same as (*B*) for macrophages from the control and day 1
760 groups. (*D*) Venn diagram showing the intersection of differentially expressed genes
761 between cells from the control and day 1 groups for stem cells, macrophages, T cells,
762 and enterocytes. (*E*) Top 10 significantly enriched gene ontology (GO) terms of 67
763 common differentially expressed genes for stem cells, macrophages, T cells, and
764 enterocytes.
765

766 **Figure 3. Dynamics and differentiation trajectories of intestinal stem cell (ISC)**
767 **subsets in irradiation-induced intestinal injury and regeneration.** (*A*) tSNE
768 projection of 2,411 ISCs identified, colored by Seurat cluster identities. (*B*) Heatmap
769 of the average expression of the selected ISC function-related marker genes in five
770 ISC clusters. (*C*) Dot plots showing the ratio of observed to expected cell numbers
771 ($R_{O/E}$) of each ISC cluster in the indicated samples, with log-transformed
772 Bonferroni-corrected *P* values in Chi-square tests. (*D*) Line charts showing the
773 average luminous density of Olfm4 in immunostaining (blue) and the fraction of
774 *Olfm4*$^{+}$ CBCs (clusters 4, 9 and 16; red) in the indicated groups. (*E*) RNA velocities
775 of ISCs from the control and day 1 groups visualized on the tSNE projection. (*F*) The
776 same as (*E*) for ISCs from the day 1 and day 3 groups. (*G*) Heatmap depicting the
777 estimated activity of top 15 regulons showing differential activation in ISCs along the
778 velocity flow from the control and day 1 groups, which is depicted by a black dashed
779 line in (*E*). Shown are normalized mean area under the curve (AUC) scores of
780 expression regulation by each transcription factor estimated in SCENIC. Cells are
781 ordered according to first principal component (PC1) coordinate to grasp the primary
782 velocity orientation. (*H*, *I*) The same as (*G*) for ISCs along the velocity flow from the
783 day 1 and day 3 groups, which is depicted by black dashed lines in the left (*H*) and
784 right (*I*) panel in (*F*).
785

786 **Figure 4. The characteristics and roles of macrophage subsets in the**
787 **irradiation-induced intestinal inflammation.** (*A*) tSNE projection of 2,926 myeloid
788 cells identified, colored by Seurat cluster identities. (*B*) Heatmap of the average
789 expression of the selected myeloid cell function-related marker genes in five myeloid
790 cell clusters. (*C*) Dot plots showing the ratio of observed to expected cell numbers of
791 each myeloid cell cluster in the indicated samples, with Bonferroni-corrected P values
792 by Chi-square tests. (*D*) Flow cytometry analyses showing the percentages of $Cd14^+$
793 inflammatory macrophages at control and 3 days post-irradiation groups. (*E*)
794 Dynamic change of the percentages of Cd14+ macrophages at control, 1, 3, 7 and 14
795 days post-irradiation groups. (*F*) Expression levels of inflammatory cytokines by
796 $Cd14^+$ and $Cd14^-$ macrophages in intestine 3 day post-irradiation. (*G*) RNA velocities
797 of four macrophage clusters visualized on the tSNE projection. (*H*, *I*) Heatmap
798 depicting the estimated activities of top 15 differentially activated regulons along the
799 velocity flow, which was depicted by black dashed lines in the right (*H*) and left (*I*)
800 panel in (*G*). Shown are normalized mean area under the curve (AUC) scores of
801 expression regulation of each transcription factor estimated by SCENIC. Cells are
802 ordered according to first principal component (PC1) coordinate to grasp the primary
803 velocity orientation.
804

805 **Figure 5. Ligand-receptor interaction between the myeloid and endothelial cells.**

806 (*A*) The weighted interaction numbers of ligand-receptor pairs between the pairwise

807 interactions of different cell types in control (top) and day 3 group (bottom). (*B*)

808 Difference of hallmark pathway activities between the C12-Endothelial cells from

809 control and day 3 groups. Shown are *t* values calculated in a linear modal comparing

810 the pathway scores estimated by gene set variation analysis (GSVA) between cells

811 from the two groups. (*C*) The same as (*B*) for C25-Endothelial cells from the control

812 and day 3 groups. (*D*) The weighted interaction intensity of inflammatory-related and

813 pro-proliferative ligand-receptor pairs between pairwise interactions of myeloid and

814 endothelial cells in control and day 3 groups.

Figure 1

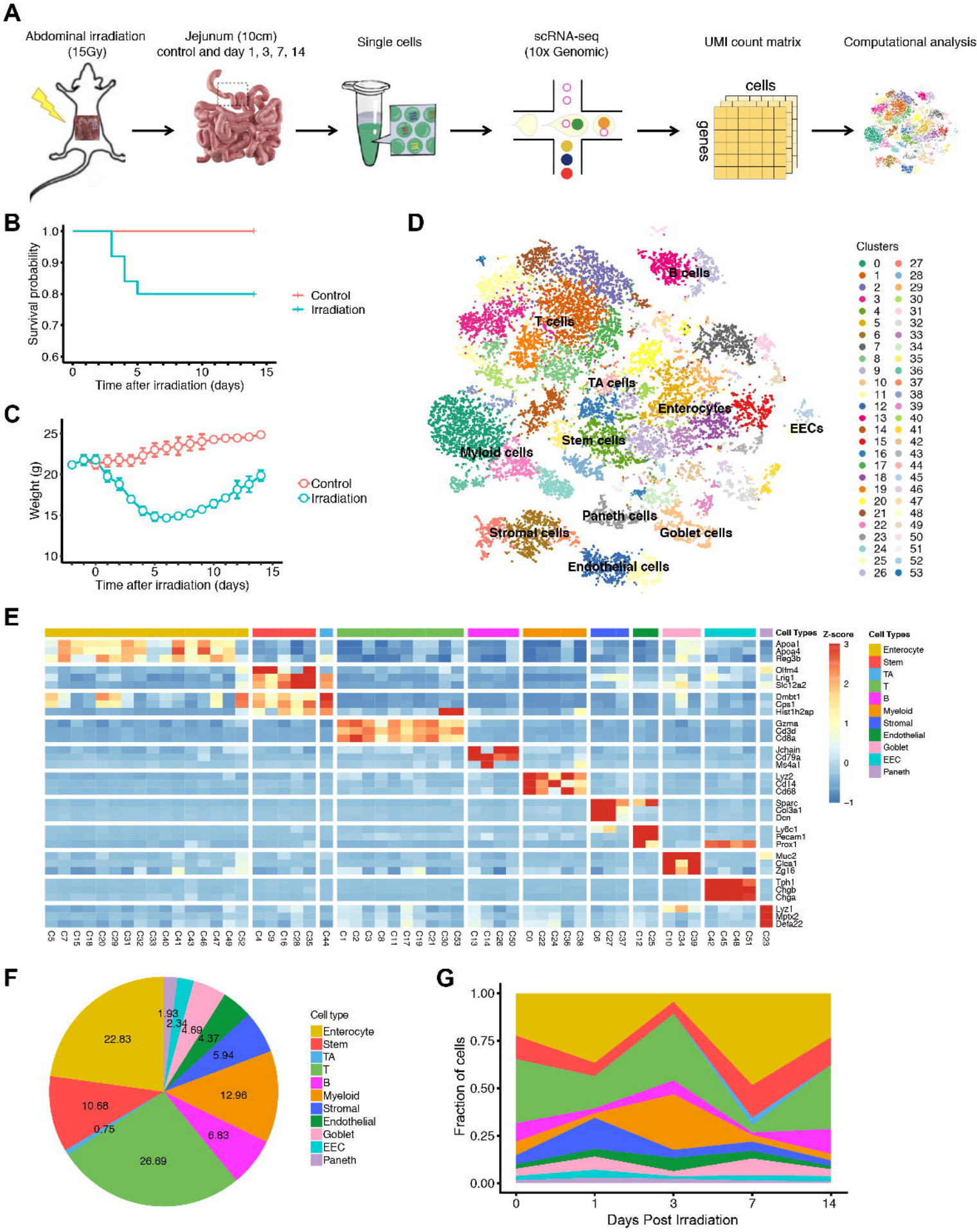
A
Abdominal irradiation (15Gy)
Jejunum (10cm) control and day 1, 3, 7, 14
Single cells
scRNA-seq (10x Genomic)
UMI count matrix
cells
genes
Computational analysis
B
Survival probability
Time after irradiation (days)
Control
Irradiation
C
Weight (g)
Time after irradiation (days)
Control
Irradiation
D
B cells
T cells
TA cells
Enterocytes
EECs
Stem cells
Myloid cells
Paneth cells
Stromal cells
Goblet cells
Endothelial cells
Clusters
E
Cell Types
Z-score
Apoa1
Apoa4
Reg3b
Olfm4
Lrig1
Slc12a2
Dmbt1
Cps1
Hist1h2ap
Gzma
Cd3d
Cd8a
Jchain
Cd79a
Ms4a1
Lyz2
Cd14
Cd68
Sparc
Col3a1
Dcn
Ly6c1
Pecam1
Prox1
Muc2
Clca1
Zg16
Tph1
Chgb
Chga
Lyz1
Mptx2
Defa22
Enterocyte
Stem
TA
T
B
Myeloid
Stromal
Endothelial
Goblet
EEC
Paneth
F
Cell type
Enterocyte
Stem
TA
T
B
Myeloid
Stromal
Endothelial
Goblet
EEC
Paneth
22.83
10.68
0.75
26.69
6.83
12.96
5.94
4.37
4.69
2.34
1.93
G
Fraction of cells
Days Post Irradiation

Figure 2

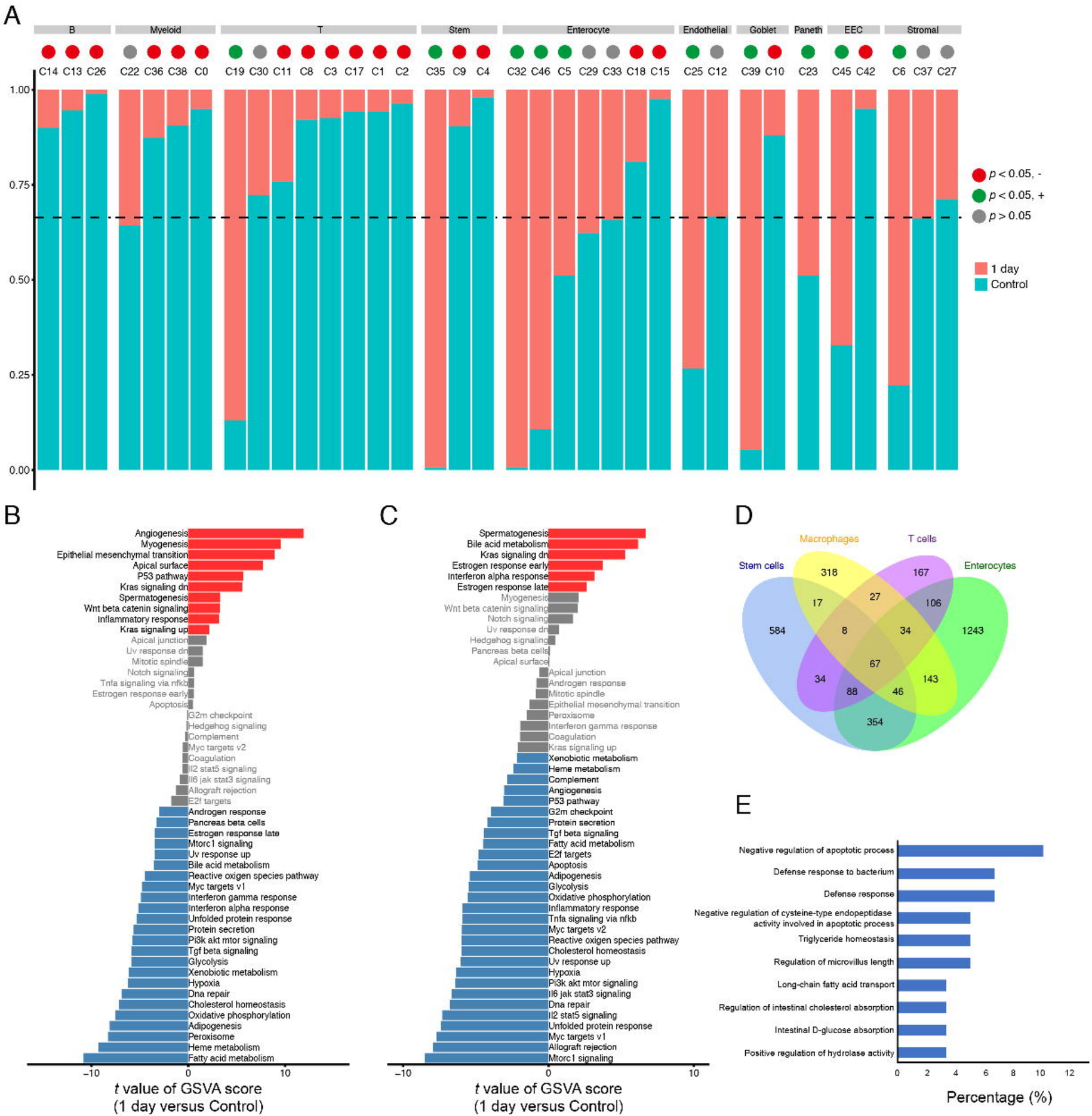
A
B
Myeloid
T
Stem
Enterocyte
Endothelial
Goblet
Paneth
EEC
Stromal
C14 C13 C26 C22 C36 C38 C0 C19 C30 C11 C8 C3 C17 C1 C2 C35 C9 C4 C32 C46 C5 C29 C33 C18 C15 C25 C12 C39 C10 C23 C45 C42 C6 C37 C27
1.00
0.75
0.50
0.25
0.00
p < 0.05, -
p < 0.05, +
p > 0.05
1 day
Control
B
Angiogenesis
Myogenesis
Epithelial mesenchymal transition
Apical surface
P53 pathway
Kras signaling dn
Spermatogenesis
Wnt beta catenin signaling
Inflammatory response
Kras signaling up
Apical junction
Uv response dn
Mitotic spindle
Notch signaling
Tnfa signaling via nfkb
Estrogen response early
Apoptosis
G2m checkpoint
Hedgehog signaling
Complement
Myc targets v2
Coagulation
Il2 stat5 signaling
Il6 jak stat3 signaling
Allograft rejection
E2f targets
Androgen response
Pancreas beta cells
Estrogen response late
Mtorc1 signaling
Uv response up
Bile acid metabolism
Reactive oxigen species pathway
Myc targets v1
Interferon gamma response
Interferon alpha response
Unfolded protein response
Protein secretion
Pi3k akt mtor signaling
Tgf beta signaling
Glycolysis
Xenobiotic metabolism
Hypoxia
Dna repair
Cholesterol homeostasis
Oxidative phosphorylation
Adipogenesis
Peroxisome
Heme metabolism
Fatty acid metabolism
−10
0
10
t value of GSVA score
(1 day versus Control)
C
Spermatogenesis
Bile acid metabolism
Kras signaling dn
Estrogen response early
Interferon alpha response
Estrogen response late
Myogenesis
Wnt beta catenin signaling
Notch signaling
Uv response dn
Hedgehog signaling
Pancreas beta cells
Apical surface
Apical junction
Androgen response
Mitotic spindle
Epithelial mesenchymal transition
Peroxisome
Interferon gamma response
Coagulation
Kras signaling up
Xenobiotic metabolism
Heme metabolism
Complement
Angiogenesis
P53 pathway
G2m checkpoint
Protein secretion
Tgf beta signaling
Fatty acid metabolism
E2f targets
Apoptosis
Adipogenesis
Glycolysis
Oxidative phosphorylation
Inflammatory response
Tnfa signaling via nfkb
Myc targets v2
Reactive oxigen species pathway
Cholesterol homeostasis
Uv response up
Hypoxia
Pi3k akt mtor signaling
Il6 jak stat3 signaling
Dna repair
Il2 stat5 signaling
Unfolded protein response
Myc targets v1
Allograft rejection
Mtorc1 signaling
−10
0
10
t value of GSVA score
(1 day versus Control)
D
Macrophages
T cells
Stem cells
Enterocytes
318
167
17
27
106
584
8
34
1243
67
34
143
88
46
354
E
Negative regulation of apoptotic process
Defense response to bacterium
Defense response
Negative regulation of cysteine-type endopeptidase activity involved in apoptotic process
Triglyceride homeostasis
Regulation of microvillus length
Long-chain fatty acid transport
Regulation of intestinal cholesterol absorption
Intestinal D-glucose absorption
Positive regulation of hydrolase activity
0
2
4
6
8
10
12
Percentage (%)

Figure 3

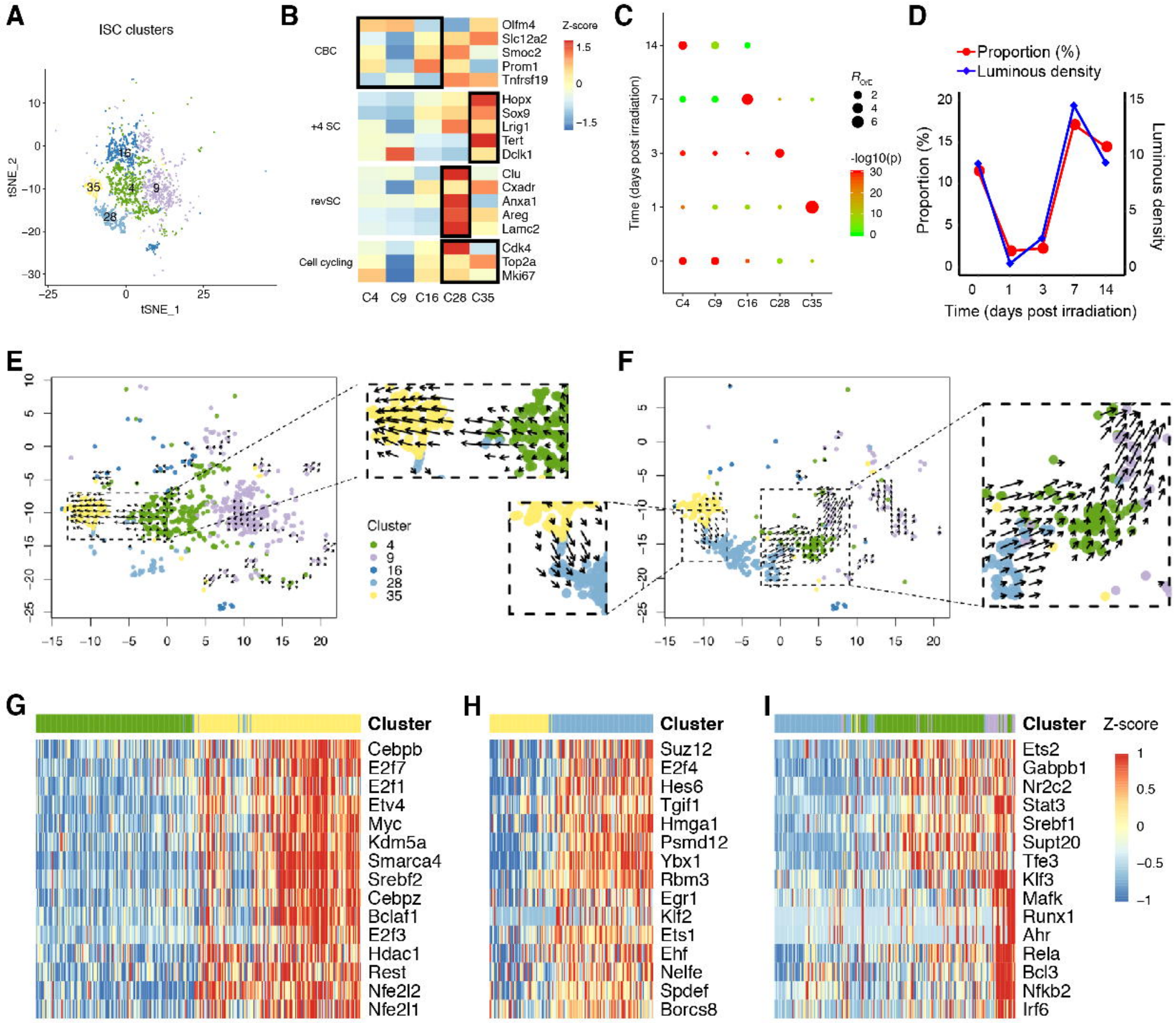
A
ISC clusters
tSNE_1
tSNE_2
B
CBC
+4 SC
revSC
Cell cycling
Olfm4
Slc12a2
Smoc2
Prom1
Tnfrsf19
Hopx
Sox9
Lrig1
Tert
Dclk1
Clu
Cxadr
Anxa1
Areg
Lamc2
Cdk4
Top2a
Mki67
Z-score
C4 C9 C16 C28 C35
C
Time (days post irradiation)
-log10(p)
D
Proportion (%)
Luminous density
Time (days post irradiation)
E
Cluster
4
9
16
28
35
F
G
Cluster
Cebpb
E2f7
E2f1
Etv4
Myc
Kdm5a
Smarca4
Srebf2
Cebpz
Bclaf1
E2f3
Hdac1
Rest
Nfe2l2
Nfe2l1
H
Cluster
Suz12
E2f4
Hes6
Tgif1
Hmga1
Psmd12
Ybx1
Rbm3
Egr1
Klf2
Ets1
Ehf
Nelfe
Spdef
Borcs8
I
Cluster
Z-score
Ets2
Gabpb1
Nr2c2
Stat3
Srebf1
Supt20
Tfe3
Klf3
Mafk
Runx1
Ahr
Rela
Bcl3
Nfkb2
Irf6

Figure 4

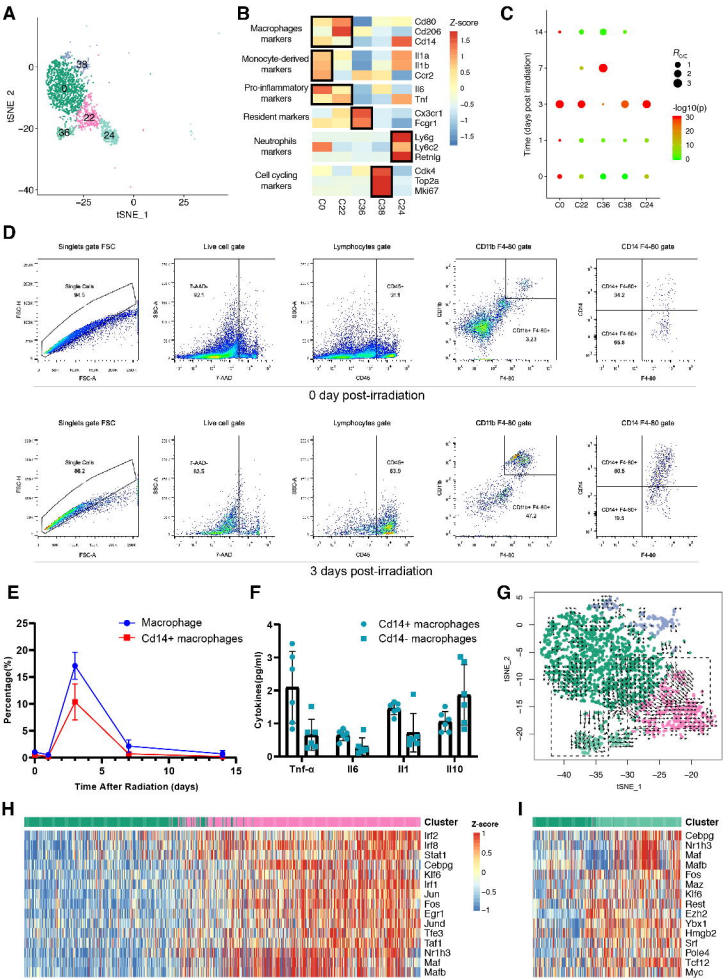
A
tSNE_2
tSNE_1
33
22
36
24
B
Macrophages markers
Monocyte-derived markers
Pro-inflammatory markers
Resident markers
Neutrophils markers
Cell cycling markers
Cd80
Ccl2/06
Cd14
Il1a
Il1b
Ccr2
Il6
Tnf
Cx3cr1
Fcgr1
Ly6g
Ly6c2
Retnlg
Cdk4
Top2a
Mki67
Z-score
C0
C22
C36
C38
C24
C
Time (days post irradiation)
Rcc
-log10(p)
D
Singlets gate FSC
Live cell gate
Lymphocytes gate
CD11b F4-80 gate
CD14 F4-80 gate
0 day post-irradiation
3 days post-irradiation
E
Macrophage
Cd14+ macrophages
Percentage(%)
Time After Radiation (days)
F
Cd14+ macrophages
Cd14- macrophages
Cytokines(pg/ml)
Tnf-α
Il6
Il1
Il10
G
tSNE_1
tSNE_2
H
Cluster
Z-score
Irf2
Irf8
Stat1
Cebpg
Klf6
Irf1
Jun
Fos
Egr1
Jund
Tfe3
Taf1
Nr1h3
Maf
Mafb
I
Cluster
Cebpg
Nr1h3
Maf
Mafb
Fos
Klf6
Maz
Rest
Ezh2
Ybx1
Hmgb2
Srf
Pole4
Tcf12
Myc

Figure 5

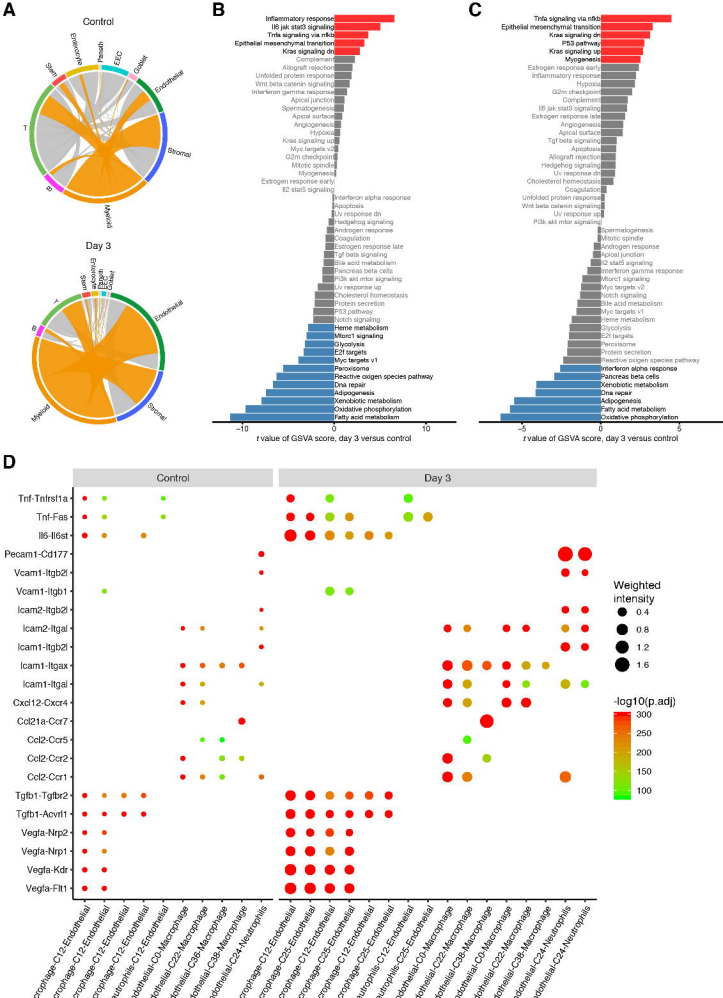
A
Control
Day 3
Epithelial
Stromal
Myeloid
B
Inflammatory response
Il6 jak stat3 signaling
Tnfa signaling via nfkb
Epithelial mesenchymal transition
Kras signaling dn
Heme metabolism
Mtorc1 signaling
Glycolysis
E2f targets
Myc targets v1
Peroxisome
Reactive oxigen species pathway
Dna repair
Adipogenesis
Xenobiotic metabolism
Oxidative phosphorylation
Fatty acid metabolism
r value of GSVA score, day 3 versus control
C
Tnfa signaling via nfkb
Epithelial mesenchymal transition
Kras signaling dn
P53 pathway
Kras signaling up
Myogenesis
Pancreas beta cells
Xenobiotic metabolism
Dna repair
Adipogenesis
Fatty acid metabolism
Oxidative phosphorylation
r value of GSVA score, day 3 versus control
D
Control
Day 3
Tnf-Tnfrsf1a
Tnf-Fas
Il6-Il6st
Pecam1-Cd177
Vcam1-Itgb2l
Vcam1-Itgb1
Icam2-Itgb2l
Icam2-Itgal
Icam1-Itgb2l
Icam1-Itgax
Icam1-Itgal
Cxcl12-Cxcr4
Ccl21a-Ccr7
Ccl2-Ccr5
Ccl2-Ccr2
Ccl2-Ccr1
Tgfb1-Tgfbr2
Tgfb1-Acvrl1
Vegfa-Nrp2
Vegfa-Nrp1
Vegfa-Kdr
Vegfa-Flt1
Weighted intensity
0.4
0.8
1.2
1.6
-log10(p.adj)
300
250
200
150
100
C0-Macrophage-C12-Endothelial
C22-Macrophage-C12-Endothelial
C38-Macrophage-C12-Endothelial
C24-Neutrophils-C12-Endothelial
C12-Endothelial-C0-Macrophage
C12-Endothelial-C22-Macrophage
C12-Endothelial-C38-Macrophage
C12-Endothelial-C24-Neutrophils
C0-Macrophage-C25-Endothelial
C22-Macrophage-C25-Endothelial
C38-Macrophage-C25-Endothelial
C24-Neutrophils-C25-Endothelial
C12-Endothelial-C25-Endothelial
C25-Endothelial-C0-Macrophage
C25-Endothelial-C22-Macrophage
C25-Endothelial-C38-Macrophage
C25-Endothelial-C24-Neutrophils